OPEN ACCESS
IOP Publishing | International Atomic Energy Agency
Nuclear Fusion
Nucl. Fusion **66** (2026) 116003 (17pp)
https://doi.org/10.1088/1741-4326/ae5f32

Overview of Wendelstein 7-X high-performance operation

O. Grulke[1,22,*], G. Acton[1], J. Adamek[41], D. Aggelis[42], R.-M. Alamo-Calderon[70], C. Albert[14], P. Aleynikov[1], K. Aleynikova[1], A. Alonso[43], G.C. Amanekwe[9], G. Anda[37], T. Andreeva[1], E. Andrew[1], A. Arkuszewski[4], S. Arnold[1], M. Arranz[43], M. Arvanitou[19], E. Ascasibar[43], M. Astrain Etxezarreta[2], O. Asztalos[37,63], K. Avramidis[67], E. Aymerich[27], A. Baciero[43], J.-P. Bähner[1], S.-G. Baek[12], M. Balden[2], J. Baldzuhn[1], S. Ballinger[65], M. Banduch[1], S. Bannmann[1], A. Bañon Navarro[2], L. Baylor[17], A. Benndorf[1], C.D. Beidler[1], D. Beiersdorf[1], M. de Beij[69], M. van Berkel[69], N. Bertelli[20], C. Biedermann[1], B. Bieg[62], T.M. Biewer[17], G. Birkenmeier[2], L. Björk[1], B. Blackwell[23], H. Blank[2], T. Bluhm[1], D. Böckenhoff[1], D. Boeyaert[35], D. Bold[1], A. Bonciarelli[1], G. Bongiovi[7], M. Borchardt[1], D. Borodin[38], T. Bosman[44], Y. Boumendjel[35], H. Bouvain[1], S. Bozhenkov[1], T. Bräuer[1], C. Brandt[1], S. Brezinsek[38], K.J. Brunner[1], A. Buhler[2], S. Buller[30], L. Burton[21], C. Büschel[1], R. Bussiahn[1], B. Buttenschön[1], A. Buzás[37], V. Bykov[1], J. Cai[38], I. Calvo[43], A. Cappa[43], A. Carls[1], F. Carovani[1], M. Carr[45], D. Carralero[43], T. Carroll[20], B.B. de Carvalho[6], J.R. Casas[26], D. Castano-Bardawil[9], J. Cavalier[41], R. Cavazzana[57], N. Chaudhary[1], I. Chelis[67], D. Cipciar[1], G. Conway[2], F. Cordella[48], Y. Corre[46], P. Costello[1], K. Crombé[9,51], G. Cseh[37], B. Csillag[2], H.I. Cu Castillo[2], G. Czymek[38], H. Damm[1], R.J. Davies[1], S. Degenkolbe[1], W. Dekeyser[47], L. Delgado-Aparicio[20], A. Demby[35], C. Desgranges[46], C.-P. Dhard[1], A. Dinklage[1,29], T. Dittmar[38], L. Dittrich[1], S. Dräger[1], M. Dreval[5], M. Drevlak[1], J. Droste[29], R.K. Duligal[44], P. Dumortier[9], D. Dunai[37], E. Edlund[49], A. Edmondson[35], P. van Eeten[1], G. Ehrke[1], M. Endler[1], D.A. Ennis[39], F.J. Escoto[43], T. Estrada[43], B. Faber[35], F. Federici[45], J. Fellinger[1], Y. Feng[1], D.L. Fernando[2], S. Fischer[1], O.P. Ford[1], T. Fornal[4], J. Frank[1,21], H. Frerichs[35], G. Fuchert[1], K. Fujii[17], M. Fukuyama[8], J. Galdón Quiroga[25], J. Gallego Llorente[43], Y. Gao[1], K. Garcia[29], O.E. Garcia[50], M. Garcia-Munoz[25], J.M. García Regaña[43], B. Geiger[35], J. Geiger[1], P. Geißler[29], M. Gerard[35], L. Giudicotti[18], T. Gonda[39], J.C. Gonzalez[2], A. González Ganzábal[43], A. Goodman[1], A. Goriaev[9,51], D. Gradic[1], M. Grahl[1], M. Grasser[1], D. Grekov[5], E. Grelier[46], G. Grenfel[2], M. Griener[2], M. Groth[13], M. Gruca[4], F. Gudicotti[40], J.F. Guerrero Arnaiz[1], V. Haak[1], M. de Haas[20], A. Haeussler[7], A. Hakola[36], L. van Ham[1], K.C. Hammond[20], B. Hamstra[44], X. Han[35], S.K. Hansen[12], A. Harris[52], J.H. Harris[17], D. Harting[38], D. Hartmann[1], D. Hathiramani[1], E.V. Hausten[1], S. Heinrich[1], P. Helander[1,29], G. Held[35], P. Henderson[20], F. Henke[1], S.A. Henneberg[12], L. Henschke[1], F. Herold[1], H. Hillebrecht[35], E. Hinson[17], M. Hirsch[1], A. Hoffmeister[29], A. Holtz[1], S.J. Hörmann[2,19], D. Höschen[38], M. Houry[46], J. Hromadka[54], J. Hua[38], X. Huang[15], K. Hunger[2], D. Hwangbo[34], K. Ida[15], Y. Igitkhanov[7], S. Iglesias Fernandez[43], V. Igochine[2], Z. Ioannidis[68], F.A. d'Isa[57], S. Jablonski[4],

[*] Author to whom any correspondence should be addressed.

B. Jabłoński[10], M. Jakubowski[1], F. Jenko[2], A. Johansson[1], C. Johnson[20], T.C.W. van Kaathoven[44], J. Kaczmarczyk[4], S. Kajita[33], J.-P. Kallmeyer[1], H. Kasahara[15], W. Kasparek[71], C. Kawan[38], Ye.O. Kazakov[9], S.A. Keller[1], N. Kenmochi[15], W. Kernbichler[14], A.K. Kharwandikar[1], M. Khokhlov[1], C. Killer[1], A. Kirschner[38], R. Kleiber[1], C.C. Klepper[17], T. Klinger[1,29], J. Knauer[1], M. Knaup[38], A. Knieps[38], M. Kobayashi[15], G. Kocsis[37], M. Koelbl[2], Y. Kolesnichenko[3], A. Könies[1], J. Kontula[13], P. Kornejew[1], Y. Kovtun[5], M. Kozulia[5], A. Krämer-Flecken[38], M. Krause[1], T. Kremeyer[1], L. Krier[1], D.M. Kriete[39], T. Krings[38], M. Krychowiak[1], I. Ksiazek[31], M. Kubkowska[4], D. Kulla[1], Y. Kulyk[5], A. Kumar[23], F. Kunkel[1], T. Kurki-Suonio[13], I. Kuzmych[55], S. Kwak[1], L. Laguardia[27], A. Langenberg[1], H. Laqua[1], H.P. Laqua[1,29], K. Leche[71], B. Lee[53], W. Lee[1], H. Leyh[1], Y. Liang[38], L. Liao[38], M. Licchelli[1], Z. Lin[28], M. Lisaj[32], A. Litnovsky[16,38], F. Litovoli[7], J. Loizu[56], B. Lomanowski[17], R. Lopez Cansino[25], B. Lopez Miranda[43], D. Lopez-Rodriguez[9], J. Lore[17], A. Lorenz[1], J. Louwe[1], E. de la Luna[43], R. Lunsford[20], Y. Luo[38], V. Lutsenko[3], N. Maaziz[1], M. Machielsen[56], R. Mackenbach[56], M. Madeira[1], D. Makowski[10], P. Manz[29], E. Maragkoudakis[1], O. Marchuk[38], A. Marinoni[12], M. Markl[14], S. Marsen[1], J. Martinez Fernandez[43], Y. Martseniuk[5], N. Marushchenko[1], S. Masuzaki[15], S. Matsheza[21], D. Maurer[39], M. Mayer[2], D. Mazur[31], K. McCarthy[43], O. McCormack[57], P. McNeely[1], D. Medina Roque[43], J. Meineke[1], S. Meitner[17], A. Menzel-Barbara[1], B. van Milligen[43], S. Misdanitis[42], A. Mishchenko[1], R. Mitteau[46], E. Moeyaert[47], A.I. Mohammed[20], V.E. Moiseenko[5,64], A. Möller[1], S. Möller[38], B. Molnar[37], V. Moncada[46], D. Morfin-Guerrero[21], M.C.L. Morren[44], D. Moseev[1], G. Motojima[15], S. Mulas[43], P. Mulholland[44], V. Murugesan[1], M. Nagel[1], D. Nagy[37], V. Nair[1], Y. Narbutt[1], D. Naujoks[1], H.G. Neilson[20], F. Nespoli[20], G. Neu[2], R. Neu[2], O. Neubauer[38], U. Neuner[1], S.K. Ngo[46], D. Nicolai[38], S.K. Nielsen[22], N. Nikulsin[1], T. Nishizawa[8], L. Nitzsche[1], C. Nührenberg[1], R. Ochoukov[2], G. Offermanns[38], K. Ogawa[15], J. Ongena[9], J.W. Oosterbeek[1], M. Otte[1], E. Overduin[1], N. Pablant[20], L. Pacios[43], N. Panadero[43], A. Pandey[1], K. Parks[17], G. Partesotti[1], E.A. Pasch[1], S. de Pascuale[17], R. Pavlichenko[5], A. Pavone[2], E. Pawelec[31], A. de la Pena Gomez[43], A. Pereira[43], V. Perseo[1], B. Peterson[15], F. Pisano[27], S. Pitcher[40], B. Plaum[71], G. Plunk[1], L. Podavini[1], N.S. Polei[1], P. Poloskei[1], S. Ponomarenko[1], P. Pons-Villalonga[29], A. Popov[58], M. Porkolab[12], J.H.E. Proll[1,44], M.J. Pueschel[69], A. Raak[21], R. Ragona[22], K. Rahbarnia[1], M. Rasiński[38], J. Rasmussen[22], O. Raths[1], E. Rattawongnara[1], D. Refy[37], F. Reimold[1], T. Richert[1], M. Richou[46], J. Ricken[1], J.S. Riemann[1], K. Rißе[1], J. de la Riva Villen[43], G. Roberg-Clark[1], E. Rodriguez[1], C. Rogge[1], V. Rohde[2], J. Romazanov[38], T. Romba[1], D. Rondeshagen[1], P. Rong[1], M. Rud[22], T. Rummel[1], A. Runov[1], N. Rust[1], L. Ryc[4], D. Ryndyk[38], H. Sakai[8], M. Salewski[22], E. Sanchez[43], L. Sanchis Sanchez[13], S. Satake[15], G. Satheeswaran[38], J. Schacht[1], E. Scharff[1], F. Scharmer[1], G. Schlisio[1], K. Schmid[2], B.S. Schmidt[22], G.L. Schmidt[20], O. Schmitz[35], M. Schneider[1], T. Schröder[1], R. Schroeder[1], M. Schülke[1], B. Schweer[9], S. Sereda[1], B. Shanahan[12], J. Shin[35], S. Shiraiwa[20], G. Sias[27], P. Sichta[20], F.B.T. Siddiki[35], S. Simko[35], L. Singh[35], S. Sipilae[13], C. Slaby[1], M. Ślęczka[32], B. Smith[20], D.R. Smith[35], H.M. Smith[1], J. Smoniewski[12], M. Spolaore[57,66], A. Spring[1], T. Stange[1], A. von Stechow[1], P. Steinbrunner[2], I. Stepanov[9], L. Stephey[35], U. Stroth[2,19], C. Suzuki[15], Y. Suzuki[59], C. Swee[35], L. Syrocki[4], T. Szepesi[37], M. Szymanski[4], H. Takahashi[24], N. Tamura[1], K. Tanaka[15], C. Tantos[7], S. Thiede[1], H. Thienpondt[43], H. Thomsen[1], T. Thun[1], S. Togo[34], T. Tork[1], M. Torkler[29], H. Trimiño Mora[1], A. Tsikouras[1], D. Valougeorgis[42], S. Varoutis[1], M. Vavrik[37], S. Vaz Mendes[1], M. Vecsei[1], J.L. Velasco[43], L. Versemann[1], M. Verstraeten[9], M. Vervier[9], N. Vianello[60], E. Viezzer[25], E.-M. Villalobos-Granados[1], J. Wagner[1], E. Wang[38], M. Wappl[1], F. Warmer[1], Th. Wegner[1], W. Wei[38], G. Weir[1], N. Wendler[4], A. White[12], M. Willensdorfer[2], T. Windisch[1], A. Winter[1], V. Winters[29], M. Wischmeier[2], R. de Wolf[47], R.C. Wolf[1,21], J. Wright[12], G. Wurden[11], P. Xanthopoulos[1], S. Xu[38], H. Yamada[33], X. Yan[38], J. Yang[38], Y. Yang[38], K. Ye[38],

M. Yokoyama[15], M. Yoshinuma[15], B. Zamorski[32], M. Zanini[1], M. Zarnstorff[20], D. Zhang[1], C. Zhu[61], M. Zilker[2], J. Zimmermann[1], A. Zocco[1], H. Zohm[2] and S. Zoletnik[37]

[1] Max Planck Institute for Plasma Physics, Wendelsteinstr. 1, 17491 Greifswald, Germany
[2] Max Planck Institute for Plasma Physics, Boltzmannstr. 2, 85748 Garching, Germany
[3] Institute for Nuclear Research, prospekt Nauky 47, Kyiv 03680, Ukraine
[4] Institute of Plasma Physics and Laser Microfusion, 23 Hery Str., 01-497 Warsaw, Poland
[5] Institute of Plasma Physics, National Science Center 'Kharkiv Institute of Physics and Technology', 1 Akademicheskaya St., Kharkiv 61108, Ukraine
[6] Instituto de Plasmas e Fusão Nuclear, Av. Rovisco Pais 1, 1049-001 Lisboa, Portugal
[7] Karlsruhe Institute of Technology, Kaiserstr. 12, 76131 Karlsruhe, Germany
[8] Kyushu University, 744 Motooka Nishi-ku, Fukuoka 819-0395, Japan
[9] Laboratory for Plasma Physics, LPP-ERM/KMS, Av. de la Renaissance 30, 1000 Brussels, Belgium
[10] Department of Microelectronics and Computer Science, Łódź University of Technology, Wolczanska 221/223, 93-005 Łódź, Poland
[11] Los Alamos National Laboratory, Los Alamos, NM 87545, United States of America
[12] Plasma Science and Fusion Center, Massachusetts Institute of Technology, Cambridge, MA 02139, United States of America
[13] Aalto University, Konemiehentie 1, 02150 Espoo, Finland
[14] Graz University of Technology, Rechbauerstraße 12, 8010 Graz, Austria
[15] National Institute for Fusion Science, National Institutes of Natural Sciences, 322-6 Oroshi-cho, Toki, Gifu 509-5292, Japan
[16] National Research Nuclear University MEPhI, Kashirskoe shosse, 31, 115409 Moscow, Russian Federation
[17] Oak Ridge National Laboratory, 1 Bethel Valley Rd, Oak Ridge, TN 37831, United States of America
[18] Department of Physics and Astronomy, Padova University, Via Marzolo 8, 35131 Padova, Italy
[19] Physics Department, Technical University of Munich, TUM School of Natural Sciences, James-Franck-Str. 1, 85748 Garching, Germany
[20] Princeton Plasma Physics Laboratory, 100 Stellarator Rd, Princeton, NJ 08543, United States of America
[21] Technical University of Berlin, Straße des 17. Juni 135, 10623 Berlin, Germany
[22] Department of Physics, Technical University of Denmark, Anker Engelunds Vej 1, 2800 Kgs Lyngby, Denmark
[23] The Australian National University, Acton ACT 2601, Canberra, Australia
[24] Tohoku University, 2-1-1 Katahira, Aoba Ward, Sendai, Miyagi 980-8577, Japan
[25] Department of Atomic, Molecular and Nuclear Physics, University of Sevilla, San Fernando, 4, 41004 Sevilla, Andalucía, Spain
[26] Universitat Politécnica de Catalunya. BarcelonaTech, C. Jordi Girona, 31, 08034 Barcelona, Spain
[27] University of Cagliari, Via Universitá, 40, 09124 Cagliari, Italy
[28] Department of Physics and Astronomy, University of California, 4129 Frederick Reines Hall, Irvine, CA 92697, United States of America
[29] University of Greifswald, Domstr. 11, 17489 Greifswald, Germany
[30] University of Maryland, 8125 Paint Branch Drive, College Park, MA 20742, United States of America
[31] University of Opole, plac Kopernika 11a, 45-040 Opole, Poland
[32] University of Szczecin, Aleja Papieża Jana Pawła II 22A, 70-453 Szczecin, Poland
[33] University of Tokyo, 5-1-5 Kashiwanoha, Kashiwa, Chhiab 277-0882 Japan
[34] University of Tsukuba, 1-1-1 Tennodai, Tsukuba, Ibaraki 305-8577, Japan
[35] University of Wisconsin-Madison, Engineering Drive, Madison, WI 53706, United States of America
[36] 36 VTT Technical Research Centre of Finland Ltd., P. O. Box 1000, 02044 VTT, Finland
[37] HUN-REN Centre for Energy Research, Institute for Atomic Energy Research, Konkoly-Thege Miklós út 29-33, 1121 Budapest, Hungary
[38] Institute of Fusion Energy and Nuclear Waste Management—Plasmas Physics, Wilhelm-Johnen-Straße, 52425 Jülich, Germany
[39] Auburn University, Auburn, AL 36849, United States of America
[40] ITER Organization, 8 rue Jules Horowitz, 13115 Saint-Paul-lez-Durance, France
[41] Institute of Plasma Physics of the Czech Academy of Science, U Slovanky 2525/1a, 182 00 Prague 8 Libeň, Czech Republic
[42] University of Thessaly, Argonafton & Filellinon, Volos 38221, Greece
[43] Laboratorio Nacional de Fusión, CIEMAT, Avenida Complutense 40, 28040 Madrid, Spain
[44] Eindhoven University of Technology, 5600 MB Eindhoven, Netherlands
[45] Culham Centre for Fusion Energy, Abingdon OX14 3EB, United Kingdom of Great Britain and Northern Ireland

[46] CEA Cadarache, 13115 Saint-Paul-lez-Durance, France
[47] Katholieke Universiteit Leuven, Oude Markt 13, 3000 Leuven, Belgium
[48] ENEA—Centro Ricerche Frascati, Via Enrico Fermi 45, 00044 Frascati, Italy
[49] SUNY Cortland, 21 Graham Ave, Cortland, NY 13045, United States of America
[50] Department of Physics and Technology, UiT The Arctic University of Norway, Klokkargardsbakken 35, 9019 Tromsø, Norway
[51] Department of Applied Physics, Ghent University, Sint-Pietersnieuwstraat 41 B4, 9000 Ghent, Belgium
[52] Illinois State University, 100 North University Street, Normal, IL 61761, United States of America
[53] Columbia University, 116th and Broadway, New York, NY 10027, United States of America
[54] Charles University, Ovocnýtrh 5, Prague 1, Czech Republic
[55] Karazin Kharkiv National University, Svobody Square 4, Kharkiv 61022, Ukraine
[56] École Polytechnique Fédérale de Lausanne, Swiss Plasma Center, Station 13, 1015 Lausanne, Switzerland
[57] Consorzio RFX, Corso Stati Uniti 4, 35127 Padova, Italy
[58] Ioffe Physical-Technical Institute of the Russian Academy of Sciences, 26 Politekhnicheskaya, St Petersburg 194021, Russian Federation
[59] Hiroshima University, 1-5-1 Kagamiyama, Higashi-Hiroshima 739-8529, Japan
[60] Consiglio Nazionale delle Ricerche, Piazzale Aldo Moro 7, 00185 Roma, Italy
[61] University of Science and Technology of China, No.96, JinZhai Road Baohe District, Hefei, Anhui 230026, China
[62] Politechnika Morska w Szczecinie, Zakład Fizyki ul. Wały Chrobrego 1-2, 70-500 Szczecin, Poland
[63] Department of Nuclear Energy, Faculty of Natural Sciences, Budapest University of Technology and Economics, Műegyetem rakpart 3, 1111 Budapest, Hungary
[64] Uppsala University, Box 65, 75103 Uppsala, Sweden
[65] Commonwealth Fusion Systems, 117 Hospital Rd, Devens, MA 01434, United States of America
[66] Institute for Plasma Science and Technology, Corso Stati Uniti 4, 35127 Padova, Italy
[67] Department of Physics, National and Kapodistrian University of Athens, Zografou University Campus, 15784 Athens, Greece
[68] Department of Aerospace Science and Technology, National and Kapodistrian University of Athens, 34400 Psachna, Greece
[69] Dutch Institute for Fundamental Energy Research, P.O. Box 6336, 5600 HH Eindhoven, Netherlands
[70] Pontificia Universidad Católica del Perú, 1801 Universitaria Avenue, San Miguel Lima 32, Peru
[71] Institute of Interfacial Process Engineering and Plasma Technology, Pfaffenwaldring 31, 70569 Stuttgart, Germany

E-mail: olaf.grulke@ipp.mpg.de

Received 6 January 2026, revised 16 March 2026
Accepted for publication 14 April 2026
Published 14 May 2026

Abstract

The Wendelstein 7-X (W7-X) stellarator has completed two consecutive experimental campaigns OP 2.2 (Sep.-Dec. 2024) and OP 2.3 (Feb.-May 2025) under a new operational strategy enabling more than one year of uninterrupted device availability. This approach, supported by exceptionally high subsystem reliability, allowed sustained high-efficiency plasma operations with up to 80–100 discharges per day across a broad range of magnetic configurations. Several key technical upgrades-most notably the first operation of a 1.5 MW class steady-state gyrotron, a new steady-state pellet injector, and advanced real-time feedback control systems significantly enhanced heating, fueling, and plasma control capabilities. Together, these improvements enabled major advances in long-pulse performance, high-β operation, and confinement optimization. Long-pulse discharges achieved 1.8 GJ of injected energy under fully detached divertor conditions, while reduced-field scenarios facilitated record volume-averaged β values approaching 3%. High-performance plasmas with centrally peaked density profiles, created via neutral beam injection (NBI) or sustained pellet fueling, demonstrated strongly reduced turbulent transport and stellarator-record fusion triple products. Complementary studies of power exhaust and divertor heat loads revealed the role of scrape-off-layer drift physics in shaping strike-line patterns under attached conditions. Together, the results from OP 2.2 and OP 2.3 significantly expand the operational space of W7-X and strengthen its role as a leading platform for steady-state stellarator research and reactor-relevant plasma scenarios.

Keywords: magnetic confinement, stellarator, Wendelstein 7-X

(Some figures may appear in colour only in the online journal)

1. Introduction

The Wendelstein 7-X (W7-X) stellarator has recently completed two experimental campaigns, OP 2.2 and OP 2.3, carried out over the last two years. These campaigns marked the first implementation of a revised operational strategy, designed to maximize experimental efficiency by reducing commissioning overhead. Instead of conducting a full time-consuming recommissioning before each phase, a single commissioning period preceded two full three-month experimental campaigns. Between phases, a short maintenance phase is introduced, however neither the cryogenic system was warmed up nor the plasma vessel vented, thereby enabling a direct transition between operational periods. This approach required comprehensive scientific planning and placed high demands on the technical reliability of the device and exceptional performance from key subsystems, which need to be in full operation for longer than one year. The W7-X components demonstrated reliability well beyond expectations, with failure rates below 1%. This stability was crucial for supporting long campaign durations and consistent experimental conditions. Plasma operation was carried out in both campaigns without major issues. Typically, 80–100 scientific discharges were performed per day across a broad range of magnetic field configurations, representing an improvement also in terms of execution efficiency. Several major technical upgrades were implemented prior to OP 2.2 to further strengthen operational capabilities. These included the prototype operation of a high-power gyrotron (1.3 MW steady-state at a frequency of $f = 140$ GHz) [1], the installation of a steady-state pellet injector [2], improvements to multiple diagnostic systems, and enhancements of plasma feedback control systems. The latter incorporated plasma radiation feedback, electron cyclotron resonance heating (ECRH) power stabilization, and plasma density control via ECRH. The scientific program of OP 2.2 and OP 2.3 was directed toward high-performance plasma operation. Key objectives included the extension of discharge duration, improvement of plasma confinement, and exploration of high-beta regimes. Complementary studies addressed power exhaust, with detailed investigations of the scrape-off layer (SOL) and divertor heat loads, in particular the influence of drift effects on divertor strike-line patterns. Together, these campaigns advanced both the technical and scientific basis of W7-X, consolidating its role as the leading device for steady-state stellarator research. The paper is organized as follows: In section 2 the key enhancements are introduced. Section 3 outlines the progress of long-pulse operation, before the key findings of operation at high plasma-β in section 4, improved confinements in section 5, and divertor heat load studies in section 6 are summarized.

2. Enhancements and operation overview

In preparation for future high-performance, steady-state operation, W7-X has initiated a comprehensive upgrade strategy aimed at enhancing both plasma heating capabilities and particle fueling systems. These developments are critical to supporting plasma discharges lasting up to 30 minutes at elevated performance levels. The extension of plasma heating power follows a dual approach, targeting upgrades to both the neutral beam injection (NBI) and ECRH systems over the coming years. At the current stage, ECRH upgrades focus on the deployment of high-power gyrotrons up to a power of 2 MW, capable of delivering increased reliable steady-state power levels of at least 1 MW. A first prototype of a 1.5 MW-class gyrotron has been successfully operated during the last two experimental campaigns. Compared to the original design of the 1 MW W7-X gyrotrons, the upgraded tube incorporates a resonator with a larger diameter and operates in the $TE_{28,10}$ mode. Together with the improved cooling systems, this enables enhanced power loading on internal gyrotron components. As shown in figure 1, which presents a photograph of the gyrotron alongside power measurements on a matched test load, the output power is limited to 1.3 MW by the onset of parasitic oscillations near 122.5 GHz and 135 GHz. These oscillations degrade the electron beam quality, reducing beam-wave interaction efficiency and generating additional intrinsic stray radiation within the gyrotron. As a countermeasure, the next gyrotron will have an improved beam tunnel. During plasma operation, the gyrotron was routinely operated at an output power of 1.1 MW without any issues.

In parallel with heating system enhancements, a new screw-type pellet injector has been developed to meet the demanding particle fueling requirements of long-pulse operation [2]. This injector is capable of delivering hydrogen or deuterium pellets with variable diameters ranging from 2 mm to 3 mm. The injection velocity can be precisely controlled within the range of 400–600 m s^{-1}, and the system supports repetition rates of up to 5 Hz. The design emphasizes compatibility with W7-X's long-pulse mission by enabling continuous operation over extended discharge durations of up to 30 minutes. This is achieved through a robust drive mechanism and active cooling of critical components, ensuring thermal and mechanical stability during prolonged use. Due to the injector's flexibility in pellet size and injection parameters, it is planned to integrate the pellet fueling into the real-time peak density control system in the near future. While feedback systems are not fundamentally required for plasma control in stellarators due to their intrinsic steady-state magnetic configurations, W7-X has significantly enhanced its feedback control capabilities to enable precise and reproducible scientific and

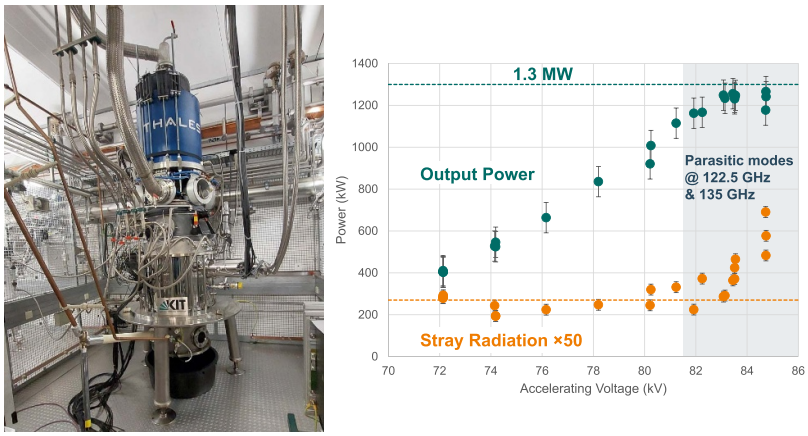

Figure 1. Photograph of the new 1.5 MW gyrotron in its final location (left) and measurement of the gyrotron output power onto a test load vs its acceleration voltage.

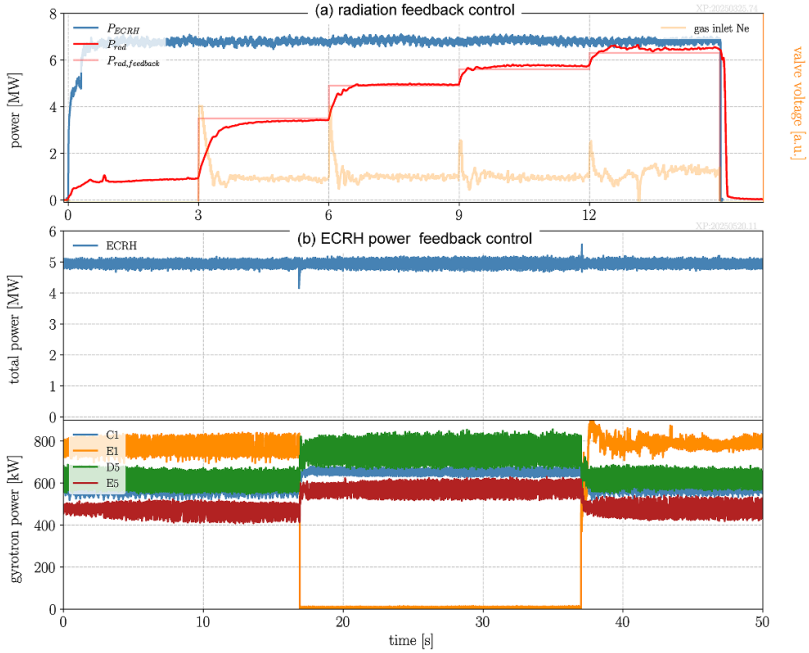

Figure 2. Examples of newly established feedback control systems: (*a*) Seeded radiation feedback control, (*b*) ECRH power stabilization feedback control.

long-pulse operation. A new feedback control system has been implemented to regulate total plasma radiation by actively controlling impurity seeding rates. The system utilizes measurements from the bolometry diagnostic to assess total radiated power and adjusts the seeding gas injection accordingly to maintain a desired radiation level. Figure 2(*a*) illustrates a representative discharge in which the target radiation level is increased in a stepwise fashion from 3.5 MW to 6.2 MW. Neon was used as the seeding gas, and the feedback system modulated the seeding valve voltage to achieve each desired radiation level. The agreement between the target and measured radiation is excellent, demonstrating the system's effectiveness. This capability has been employed both scientifically for studies of impurity-seeded detachment and operationally, to reduce localized power loads on divertor target plates during long-pulse discharges.

Operational experience from earlier W7-X campaigns revealed that long-pulse discharges at elevated ECRH power levels are occasionally interrupted by spontaneous failure of individual gyrotrons. These unanticipated power losses lead to undesired variations of the operation parameters. To address this, a new ECRH power stabilization system was implemented. When a gyrotron trips, the system compensates in real time by increasing the output power of the remaining operational gyrotrons, thereby stabilizing the total injected ECRH power. Figure 2(*b*) shows an example of this stabilization strategy for a subset of gyrotrons. In the illustrated case, gyrotron E1 experiences a temporary dropout during the time interval $t = 17$–36 s. In response, the power outputs of the remaining gyrotrons are increased accordingly, successfully maintaining a constant total heating power throughout the dropout period. This approach ensures uninterrupted

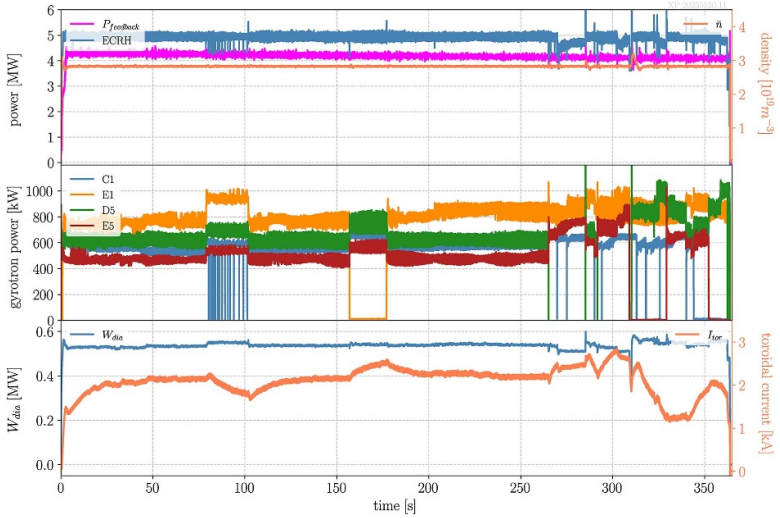

Figure 3. Overview of long-pulse operation reaching a total energy turnaround of 1.8 GJ. Shown are time traces of the total ECR heating power together with the feedback-controlled radiation power and mean plasma density (top), a selection of individual gyrotron power levels (middle), and the achieved diamagnetic energy and total toroidal current (bottom).

plasma heating and enhances the robustness of long-pulse operation.

3. Long pulse operation

W7-X is designed for long-pulse operation with plasma discharges of up to 30 min duration and a total heating energy of 18 GJ. This is facilitated by the superconducting magnetic field coils and water-cooled plasma-facing components (PFC). However, the development of localized hot spots and potential leading edges can cause excessive heat fluxes, particularly at the divertor, which may exceed its design specifications. For this reason, a step-wise operational approach has been pursued: during campaign OP 2.1, a heating energy of 1.3 GJ was successfully reached [3]. This specification value was increased to 2 GJ during the last campaigns OP 2.2 and OP 2.3, with the intention of gradually approaching the design limits in the upcoming operation campaigns. A steady-state scenario was developed with the potential for further increases in heating energy and consists of several elements: To mitigate convective heat loads on the PFCs, the divertor was operated in a detached state, achieved via feedback-controlled impurity seeding. The ECRH was applied in X2 polarization, which provides excellent single-pass absorption and prevents ECRH power deposition on the beam dump. To stabilize the strike line position on the divertor, counter-electron cyclotron current drive (ECCD) [4] was employed, thereby compensating the bootstrap current and maintaining a small net toroidal current. Figure 3(top) shows time traces of the ECR heating power, plasma radiation power, and plasma density. A discharge length of 363 s was achieved with nearly constant heating and radiation power levels. The plasma density, regulated via feedback control, remained constant throughout the discharge. Throughout the paper, unless otherwise denoted, we use the mean plasma density, defined as the line-integrated plasma density as measured by interferometry divided by the length of the sight line through the plasma n_{dl}/L. The constant ECRH power was the result of successful power stabilization feedback. Although sporadic gyrotron dropouts occurred during the pulse, these were compensated by corresponding increases in power from other gyrotrons, see figure 3 (middle). The diamagnetic energy W_{dia} remained steady, while the toroidal plasma current was consistently maintained below 3 kA, figure 3 (bottom). Beginning at $t = 270$ s, strong fluctuations in the power of individual gyrotrons were observed. These fluctuations became increasingly frequent and ultimately led to the termination of the discharge at 363 s. At this point, a total heating energy of 1.8 GJ had been achieved. Despite the premature termination of the discharge, the developed scenario was successful in maintaining low PFC heat fluxes and convective divertor loads below 3.5 MWm^{-2}. The observed fluctuations in gyrotron power were traced back to cooling issues in the ECRH beamline, which caused elevated component and air temperatures. This led to an increasing rate of arcing events in the ECRH beamline and ultimately to the discharge termination. For the upcoming campaign, improvements to the cooling system are planned to prevent a recurrence of this limitation.

4. Operation at high plasma-β

W7-X is designed for improved magnetohydrodynamic (MHD) stability at high plasma-β, with target values up to 4%, consistent with reactor requirements of the HELIAS line [5, 6]. In this context, the confinement of energetic ions, which mimic α-particle behavior in a stellarator reactor, is a crucial performance metric. Numerical simulations predict that fast ion losses decrease strongly with rising plasma-β [7]. Demonstrating high-β operation is therefore an important step toward reactor-relevant validation. From fundamental confinement scaling arguments, achieving such conditions would require very high heating powers, which are not available at W7-X. However, according to the ISS04 stellarator

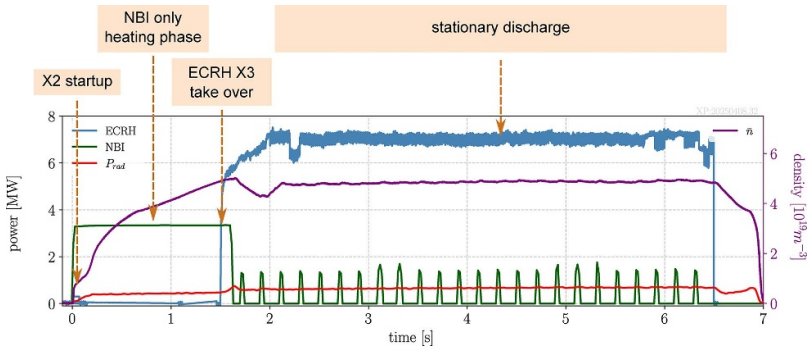

Figure 4. Demonstration of plasma operation at reduced field with ECR heating in X3 polarization. Shown are the time traces of the ECR and NBI heating powers together with the mean plasma density. The different phases of the discharge—startup, NBI heating, and X3 takeover—are indicated.

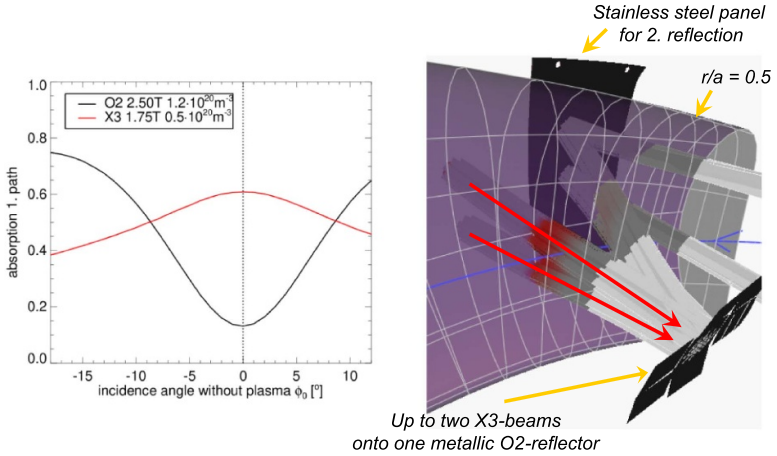

Figure 5. (left) Comparison of the dependence of ECRH absorption on incidence angle between O2 polarization at a magnetic field of $B = 2.5$ T and X3 polarization at $B = 1.75$ T. (right) Schematic of the ECRH heating beam paths. The beams are entering along the red arrows.

confinement scaling, the dependence of the confinement on magnetic field strength is weaker than on plasma β. This insight allows high-β operation to be made accessible by reducing the magnetic field strength, thereby relaxing the heating power requirements. The primary heating system at W7-X is the ECRH system at 140 GHz, which can be also applied in X3 polarization at a magnetic field of $B = 1.7$ T. However, direct plasma startup using X3 polarization is not feasible: the single-pass absorption is negligible for electron temperatures $T_e < 1$ keV, since the absorption power scales approximately as $P_{abs} \sim nT_e^2$ [8]. To overcome this, a discharge startup scheme was developed employing ECRH at 101 GHz in X2 polarization, technically limited to a short pulse, as shown in figure 4. The initial ECRH pulse generates a plasma with density $n \approx 1 \cdot 10^{19}\,\mathrm{m}^{-3}$, which is sufficient for reasonable NBI absorption. Subsequently, typically two NBI sources with a combined heating power of $P_{NBI} = 3.6$ MW are applied, leading to increased plasma density and, crucially, higher electron temperatures. Once adequate conditions are established, the remaining ECRH power in X3 polarization can take over the heating from NBI, thereby sustaining and extending the discharge. This scheme was successfully demonstrated at W7-X, enabling stable plasma operation up to 6.5 s. Because of the incomplete single-pass absorption of X3 polarization, a triple beam path scheme with the established O2-reflector tiles was used for the first experiments in OP2.2/2.3, illustrated in figure 5. In contrast to O2 heating, which exhibits strong absorption at incidence angles of $10° - 20°$ to the magnetic field, X3 heating is most efficient at perpendicular incidence, but at medium densities also safely operable with oblique incidence. This configuration effectively increases the absorption path length, enabling nearly complete absorption of the injected ECRH power and thus efficient plasma heating under reduced magnetic field conditions. A dedicated multi-pass scenario with customized reflector tiles is in preparation for OP2.4. It must be noted that the frequency limitations of the short-pulse gyrotron to $f \geqslant 101$ GHz does not match the cold X3 resonance, which is at a magnetic field of $B \approx 1.7$ T. Thus, a levitated plasma β is required to reduce the central magnetic field and allow X3 absorption on the magnetic axis.

This optimized discharge scheme yields the presently highest peak and volume-averaged plasma-β $\langle\beta\rangle$ achieved in

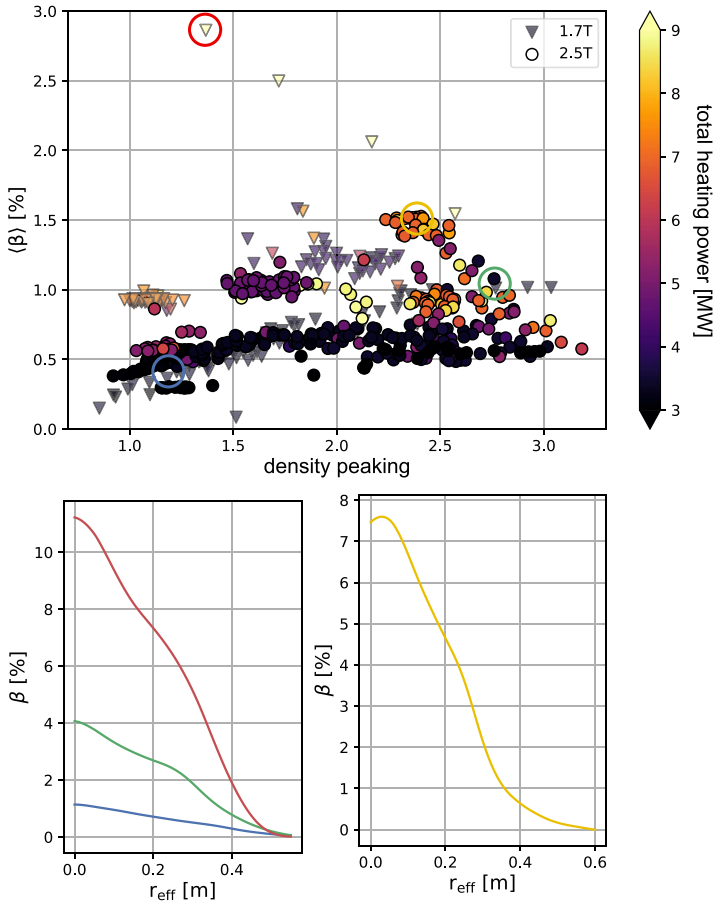

Figure 6. (top) Database study of the volume-averaged plasma-β $\langle\beta\rangle$ vs central plasma density peaking. The plasma heating power is indicated color-coded and data from two magnetic field strength $B = 1.7\,\mathrm{T}$ and $B = 2.5\,\mathrm{T}$ are displayed. (bottom) Resulting profiles of plasma-β from profile diagnostics for discharge time instants marked in the top figure.

W7-X. A database study incorporating a number of discharges at both field strengths are compiled in figure 6. An important parameter for the achieved plasma-β is the central plasma density peaking. It is generally observed that similar values of central peaking are generated at both magnetic field strengths. For similar peaking and the same range of plasma heating powers, the reduced field cases display indeed larger $\langle\beta\rangle$ values, as expected from the weak magnetic field scaling of the confinement. The radial profiles of the local plasma-β for four exemplary discharge situations are also shown in figure 6, indicated by colored circles in the database study. For the case of high magnetic field, the discharge with the so far observed best energy confinement exceeding the *ISS*04 scaling, see section 5 with a volume-averaged $\langle\beta\rangle = 1.5\%$, has the highest central values with $\beta = 7.5\%$. This value is, however, increased for the reduced magnetic field cases. In the shown examples, the radial β profiles are shown for three different values of central density peaking. Compared to the high field case, the central value is approx. 50% higher with $\beta_0 = 11\%$, though radial profiles are generally broader and result in $\langle\beta\rangle = 2.8\%$, almost a factor of two larger than the high field case. This represents the highest $\langle\beta\rangle$ value obtained in W7-X to date and highlights the importance of operating at reduced magnetic field to access high plasma-β regimes for studies of MHD stability limits and validate fast ion confinement predictions.

5. High-performance operation and advanced heating scenarios

Previous operation campaigns of W7-X have provided clear evidence that plasma confinement can be improved in discharge scenarios that employ a central peaking of the radial plasma density profile [9, 10]. This effect directly contributed to the achievement of record values of the fusion triple product in stellarator devices [11]. In these discharges, central density fueling was realized by pellet injection, which provided a localized source of particles deep in the plasma core. More recently, first indications were obtained that central density peaking can also be established using NBI [12]. In this case, the resulting centrally peaked density profile is not solely a consequence of direct NBI particle fueling. Rather, after the initial fueling phase, radial particle transport is found to be significantly reduced, thereby supporting and maintaining the central peaking of the density profile [13]. This marks an important step in broadening the operational flexibility of W7-X toward confinement-optimized scenarios. In the most

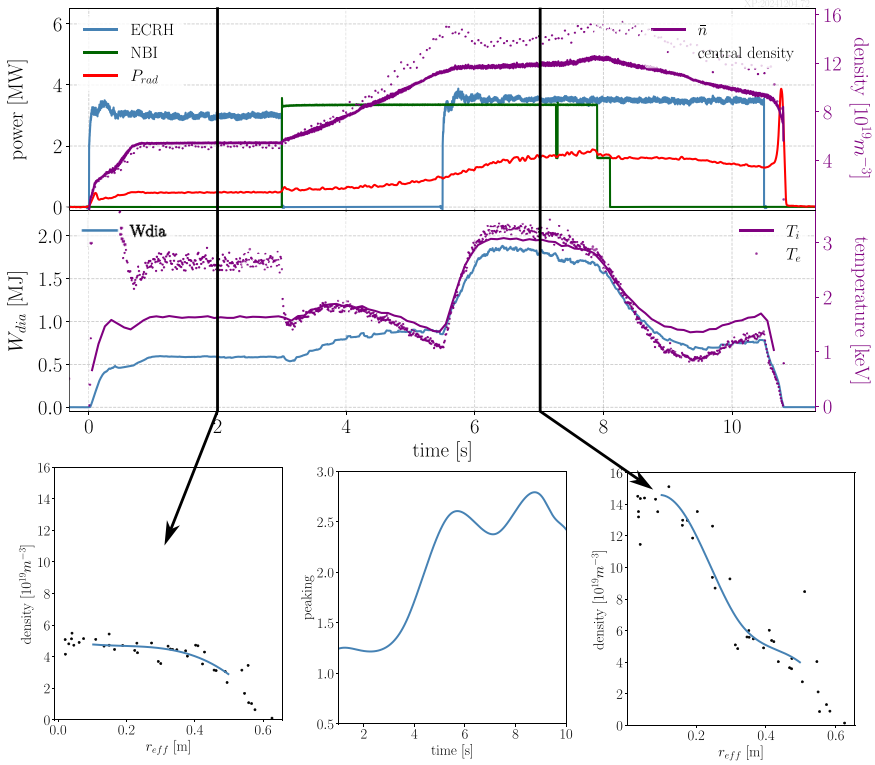

Figure 7. Discharge scenario of record fusion triple products for stellarators. The top graphs shows time traces of the ECRH and NBI heating powers together with the total radiated power P_{rad}, mean $\bar{n}$ and central plasma density traces, and the diamagnetic energy W_{dia} and central electron T_{e} and ion temperatures T_{i}. For two time instants, indicated by vertical lines in the graphs, the radial density profiles are shown at the bottom together with fits in the range $0.1\,\mathrm{m} \leqslant r_{\mathrm{eff}} \leqslant 0.5\,\mathrm{m}$. As a measure of the density profile evolution, the time trace of the ratio of core to edge ($r/a = 0.8$) density is shown, denoted as peaking.

recent campaigns, further detailed studies were conducted to tailor discharge conditions specifically toward maximizing plasma confinement and performance. Two conceptually distinct approaches were pursued: (i) discharges in which NBI heating facilitates the formation and stabilization of centrally peaked density profiles, and (ii) discharges relying on central density fueling via pellet injection. These complementary schemes provide a valuable experimental basis for understanding the interplay between fueling methods, radial transport processes, and overall stellarator confinement optimization. The typical discharge scenario for NBI-heating-induced central density peaking is illustrated in figure 7. It begins with an ECRH plasma initiated in X2 polarization at moderate heating powers and densities. The corresponding plasma density profile, shown in figure 7 at $t = 2\,\mathrm{s}$, is centrally flat and exhibits radial density gradients only in the outer region at $r_{\mathrm{eff}} > 0.4\,\mathrm{m}$. A key step for establishing central density peaking is the transition of plasma heating entirely to NBI, without any additional ECRH. In this phase, the absence of central electron heating leads to equilibrated electron and ion temperatures, albeit at relatively low ion temperature levels. During the initial NBI fueling phase, the plasma density increases over several seconds before a distinct peaking of the density profile emerges in the plasma core. Once the profile is peaked, ECRH is re-applied to provide additional plasma heating. With the added power, the electron and ion temperatures, as well as the diamagnetic energy, rise rapidly and subsequently saturate at a stationary level, which in the present case persists for approximately two seconds. In this regime, the radial density profile remains strongly peaked in the plasma center with significant gradients already at $r_{\mathrm{eff}} > 0.1\,\mathrm{m}$. The density peaking factor, defined as $p = n_{\mathrm{core}}/n_{r/a=0.8}$, exhibits a gradual increase during the NBI heating phase before saturating at values of $p \approx 2.5$. The stationary phase of elevated temperatures and stored energy is sustained as long as NBI heating is applied, which is currently limited by the maximum available NBI pulse length. The peak ion temperature reaches $T_{\mathrm{i}} \approx 3\,\mathrm{keV}$, in good agreement with what is expected from neoclassical ion heat transport [9]. This indicates that transport in this regime is strongly dominated by neoclassical processes with only little contribution by turbulent heat diffusion [14, 15], in contrast to flat-density profiles where turbulent transport remains the dominant mechanism. In the high temperature phase, the energy confinement exceeds the ISS04 scaling by typically 30%–40% [16]. It should be noted that there is a power limit of ECRH in these kinds of scenarios, beyond which the central plasma density peaking is strongly reduced due to ECRH density pump out.

The duration of the improved confinement phase has so far been limited primarily by the operational time of the NBI system. A promising strategy to extend this phase is to initiate radial density peaking through a sequence of pellet injections, which can then be maintained by subsequent NBI heating, thereby yielding a noticeable prolongation of the improved

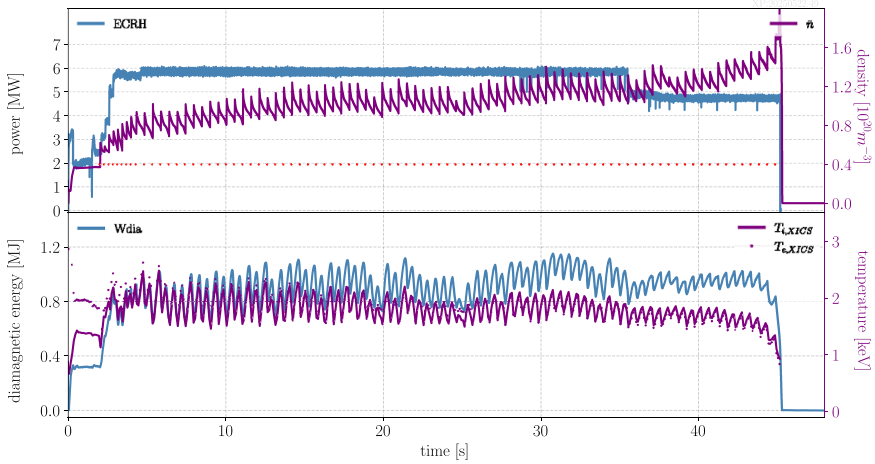

Figure 8. Example of a long-pulse high performance discharge initiated and maintained by pellet injection only. Shown are the time traces of the ECR heating power and mean plasma density (top), in which the red dots denote the time instants of pellet injection, and the diamagnetic energy and electron and ion tempratures (bottom).

confinement. To achieve sustainment over much longer timescales, however, the peaking must be supported by pellet injection alone. Such a scheme has already been demonstrated in earlier experiments [10, 17, 18], but only in a transient manner and for relatively short periods, as the previously available pellet injector was restricted to injection times of only a few seconds. With the recent availability of a new steady-state pellet injector, it is now possible to pursue this approach under substantially improved conditions, offering the prospect of sustaining the improved confinement phase for much longer durations and with greater experimental flexibility. The longest pellet-injection discharge to date is presented in figure 8. Following plasma start-up, pellet injection begins at $t = 2$ s with an initial repetition frequency of 3.5 Hz, which is later reduced to 2 Hz during the discharge. The injection times of the individual pellets are indicated by red dots in figure 8. Owing to the high plasma densities, ECR heating is applied in O2 polarization, with a constant power of 6 MW until $t = 35$ s, when the power is stepped down. Each pellet induces a modulation of the plasma density; however, the average mean density remains relatively constant at $\bar{n} \approx 1.2 \cdot 10^{20}\mathrm{m}^{-3}$. A slight upward trend in plasma density is nevertheless observed, which is partly mitigated by reducing the pellet injection frequency after 5 s. The pellet injections in this experiment are executed in a feed-forward manner. The results strongly suggest that, for longer discharge scenarios, effective control of the density will require a feedback system with variable pellet injection frequencies to stabilize the temporal density evolution, which will be realized in the near future. This is especially visible in the later phases of the discharges with reduced ECR heating power, in which the pellet fueling leads to a steady increase of the plasma density. The achieved ion temperature values, although smaller than in the combined NBI and ECRH scenario shown in figure 7, partly due to the smaller plasma heating power, are still significantly enhanced on average by 25% compared to discharges with gas fueling at similar ECR heating power levels [9, 19]. The results of both scenarios, either improved plasma performance with combined ECRH and NBI, or through a sequence of pellet injections, consistently indicate a reduction of radial heat transport. This finding is further supported by a database study for W7-X, in which the turbulent heat flux Q_{anom} is evaluated as a function of $2n\nabla T_{\mathrm{i}}$ at a given radius of $r/a = 0.4$, see figure 9(left) (adapted from Ford *et al* [12]. The normalized density gradient length a/L_n, with a denoting the minor plasma radius, is represented color-coded. Two clearly distinct regimes emerge: for small normalized density gradients, the heat flux is large and originates from a significantly higher turbulent heat diffusivity, $\chi_{\mathrm{anom}} \approx 1.2 \pm 0.5, \mathrm{m}^2\,\mathrm{s}^{-1}$. Conversely, the turbulent heat flux is considerably reduced when the normalized density gradient length is increased, yielding typical values of the turbulent heat diffusivity smaller by about a factor of five, in the range $\chi_{\mathrm{anom}} \approx 0.25 \pm 0.08, \mathrm{m}^2\,\mathrm{s}^{-1}$. It has been shown that this behavior is a feature of essentially all discharge scenarios with centrally peaked density profiles [14]. This grouping of heat flux persists even when a transition between both regimes occurs during a single discharge, for instance due to a loss of density profile peaking caused by ECRH-induced density pump-out. This result is consistent with the fundamental understanding of turbulent transport in W7-X. Both numerical simulations and experimental observations provide compelling evidence that turbulent transport in W7-X is predominantly driven by ion temperature gradient (ITG) turbulence [21–24] in ECRH-heated, gas-fueled discharge scenarios. In contrast, density-gradient-driven trapped electron mode (DTEM) transport is known to be strongly suppressed in the W7-X magnetic configuration which approaches maximum-J [25, 26], owing to the reduced regions of resonance between the diamagnetic drift and the precessional drift of trapped electrons. As a consequence, ITG turbulence in W7-X can be stabilized by density gradients without the concurrent destabilization of DTEMs, leading to improved energy confinement, elevated ion temperatures, and enhanced diamagnetic energies. This interpretation is further supported by the observed

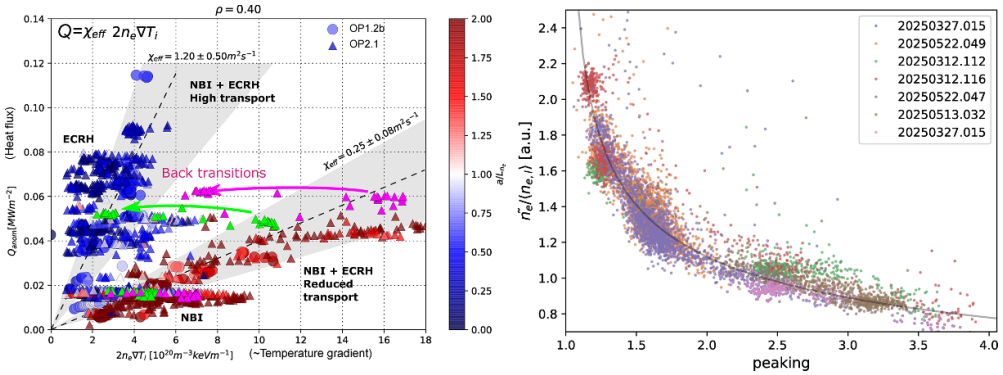

Figure 9. (left) Database analysis of the anomalous heat flux versus ion temperature gradient. The color-code denotes the density gradient length normalized to the minor plasma radius a/L_n. The dashed lines with shaded intervals denote the effective ion heat diffusivity. (right) Compilation of discharges with improved confinement phases. Shown are the relative density fluctuation degree versus the density peaking.

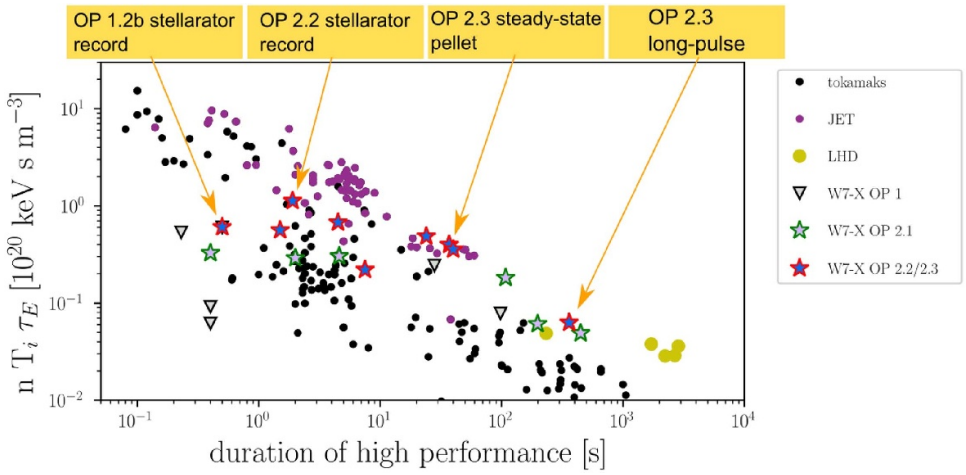

Figure 10. Compilation of the fusion triple products [20] including the newest data from JET and the last two W7-X campaigns.

dependence of the density-normalized turbulent density fluctuation magnitude as measured by phase contrast imaging [27] on the degree of density profile peaking, figure 9 (right). For a set of improved-confinement discharges including the combined ECRH and NBI scenario as well as discharges with pellet-fueling-sustained density peaking a clear anti-correlation is found between the fluctuation level and the steepness of the density profile, expressed here as the ratio of central to edge ($r/a = 0.8$) density. Density-normalized turbulence levels steeply drop when the density profile is peaked, indicating the stabilization of ITG turbulence. The improved-confinement discharges achieved in W7-X have led to unprecedented fusion triple products $nT_i\tau_E$ for stellarators. These results have been incorporated into the most recent CICLOP database and are presented in figure 10 [28]. Building on the first stellarator record for the triple product, obtained in W7-X during operational campaign OP 1.2b (2018) with pellet injection, the value was substantially increased in OP 2.2 (2024) in the combined ECRH and NBI scenario (see figure 7), reaching a maximum of $nT_i\tau_E = 1.126 \cdot 10^{20}, \mathrm{keV, s, m^{-3}}$. While these record values remain below those achieved in much larger tokamaks, W7-X performance decreases by only about 50% under the continuous pellet-fueling scheme demonstrated in OP 2.3 (2025) (see figure 8). Importantly, the resulting triple product values are comparable to those of larger tokamaks, with the added potential of extending them to much longer durations in future campaigns.

5.1. Comparison with linear numerical simulations

Linear stability simulations have been performed for the best performing discharge, figure 7. Two different time ranges in the discharge are discussed. In the $t = 1 - 3\,\mathrm{s}$ range, the plasma is heated via ECRH with a power of $P = 3\,\mathrm{MW}$. In the later phase, at $t = 6 - 8\,\mathrm{s}$, the plasma is heated with equal power $P = 3.5\,\mathrm{MW}$ by the NBI and ECRH. An intermediate phase between $t = 3\,\mathrm{s}$ and $t = 6\,\mathrm{s}$ with only NBI and reduced anomalous transport (see for example [13, 29]) is not considered here. Using the gyrokinetic code GENE [30], linear flux-tube simulations were conducted in the so-called bean flux tube in W7-X—considered to be the most unstable location—at $\rho = r_{\mathrm{eff}}/a = 0.54$ (corresponding to $r_{\mathrm{eff}} = 0.3\,\mathrm{m}$) where a denotes the minor radius of the plasma. At this value of ρ the largest density gradients are observed in the later phase combining NBI and ECRH. The relevant parameters at this position are summarized in table 1 for two different sets of gradient lengths

Table 1. Summary of the used local plasma parameters at $\rho = 0.54$ in discharge 20 241 204.72, figure 7. The gradient length scales are defined as $1/L_x = \partial_\rho \log(x)$ where x can be any of n, T_e or T_i and β is defined by the electron pressure. The collision frequency is internally defined in GENE as $\nu = 2.30 \cdot 10^{-5} \log(\Lambda)\, a[\mathrm{m}]\, n_\mathrm{e}[10^{-19}\,\mathrm{m}^{-3}] / T_\mathrm{e}^2[\mathrm{KeV}^2]$ where $\log(\Lambda)$ is the Coulomb logarithm. In the ECRH + NBI phase the two cases describe two different possible sets of gradients derived from the experimental profiles. These can be used to estimate errors stemming from the data on the type of the dominant instability.

	a/L_n	a/L_{T_e}	a/L_{T_i}	$T_\mathrm{e}/T_\mathrm{i}$	β	ν
ECRH Phase	0.39	2.73	1.74	1.13	3.28×10^{-3}	9.53×10^{-4}
ECRH + NBI Phase						
—Case 1	2.09	3.00	2.80	0.99	7.55×10^{-3}	8.26×10^{-4}
—Case 2	3.74	2.77	2.50	1.00	9.35×10^{-3}	8.18×10^{-4}

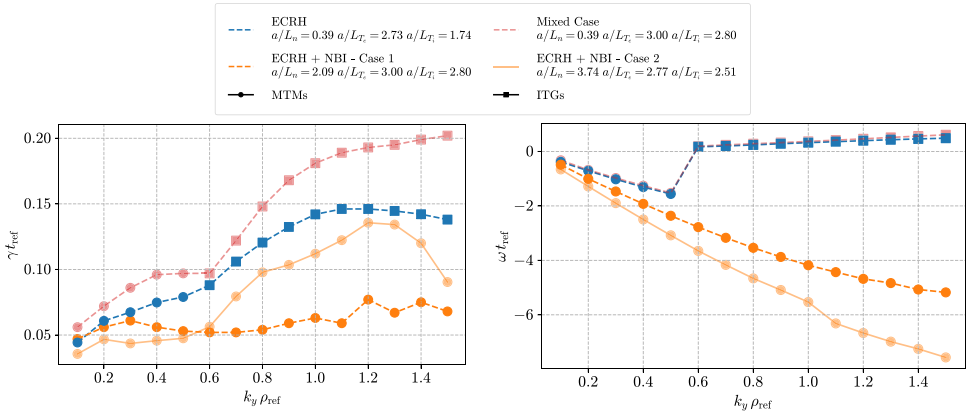

(b) Growth Rates (c) Frequencies

Figure 11. Growth rates γt_ref and frequencies ωt_ref over $k_y \rho_\mathrm{reff}$ for the parameters found from the profiles (dashed blue, dashed or solid orange, respectively) and for a mixed case with the ECRH + NBI phase temperature profiles but ECRH phase density profile (red). The dominant mode type is shown by the shape of the different data points. The dashed and solid orange lines denote two simulations which are based on different gradients both matching the same measurement data within errors. While the growth rates differ between the two cases, the same trend of stabilization of the ITG modes in the ECRH + NBI phase can be observed.

in the high performance phase. Electromagnetic effects and the parallel magnetic field fluctuations were included, the Landau–Boltzmann operator is used to model collisions. The results for a linear scan over the wavenumber from $k_y \rho_\mathrm{reff} = 0.1$ to $k_y \rho_\mathrm{reff} = 1.5$ (where ρ_reff is the ion-sound Larmor radius) are shown in figure 11. The input values found from the ECR-heated phase (see the blue curve in figure 11) result in micro tearing modes (MTMs) being the most unstable linear instability for low values of $k_y \rho_\mathrm{eff} \leqslant 0.5$. For larger values of $k_y \rho_\mathrm{eff} > 0.5$ the dominant instability is found to be an ITG mode.

In the later NBI and ECRH phase (see the orange curves in figure 11) the MTM is the dominant instability across the entire scan range of $k_y \rho_\mathrm{eff}$ due to the stabilization of the ITG mode by the higher density gradient, which counteracts any potential destabilization through an increased ion-temperature gradient. Additionally, while the MTMs would be destabilized by the increased electron temperature gradient (see red line in figure 11, and also see [29]), here the stabilizing effect of the increase in density gradient dominates. While β and ν can also act destabilizingly on the MTMs, here they do not change significantly between the two phases. Generally, the parameters in the NBI and ECRH phase lead to decreased growth rates across the range of $k_y \rho_\mathrm{eff}$, besides for $k_y \rho_\mathrm{eff} = 0.1$. It can also be seen that the result of the ITG modes being stabilized is rather robust, as the reduction in growth rate is found independent of the exact values of the changed gradients in the ECRH + NBI phase.

These linear simulation results suggest the reduction in fluctuation amplitude and turbulent fluxes in the NBI and ECRH phase due to partial stabilization of the MTMs and ITG modes from the significantly increased density gradient (compared to the moderate increase of the temperature gradients). Fully non-linear simulations are underway.

6. Divertor loads and SOL drifts

W7-X is equipped with a novel, fully water-cooled island divertor that has been specifically engineered to enable steady-state, long-pulse operation [3]. The recent heating upgrade for ECRH and NBI allowed the sustainment of higher divertor densities in attached conditions ($f_\mathrm{rad} = P_\mathrm{rad}/P_\mathrm{in} < 0.4$), for which multiple diagnostic independently measured density profiles with steeper gradients and higher fluctuation levels [31]. Heat loads were deposited on PFCs located in the target shadow region (TSR), which have a strongly reduced technical specification of allowed heat fluxes. As the data displays, heat fluxes exceed the limits of safe divertor operation in attached conditions [32], indicated in figure (see figure 12)

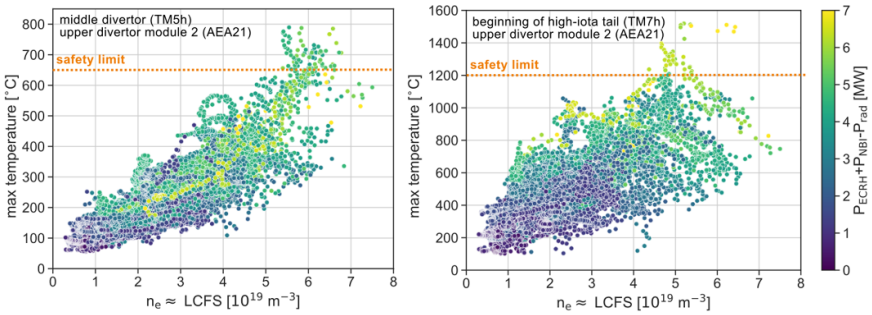

Figure 12. IR camera measurements of the maximum divertor surface temperature of the middle divertor (left) and the high-iota tail (right) of upper divertor in module 2, with respect to the density at the last closed flux surface as measured by Thomson scattering. The power entering the scrape-off layer is color-coded. The data is averaged over 200 ms and restricted to experiments in the standard magnetic configuration, with a radiated power fraction f_{rad} <0.4 and without significant density peaking, and impurity seeding.

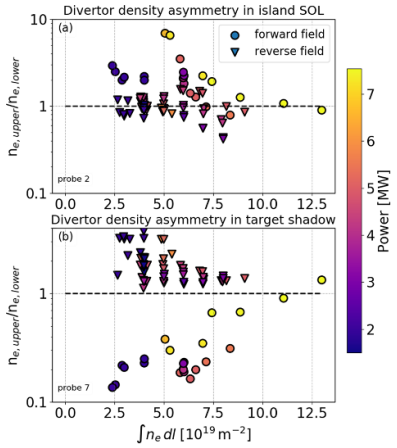

Figure 13. Ratio of electron density n_e in the upper to the lower divertor as measured by divertor Langmuir probes near (*a*) the strike line and (*b*) in the TSR. The vertical axis is logarithmic, so equal-magnitude asymmetries in opposite directions are equidistant from the black dashed line.

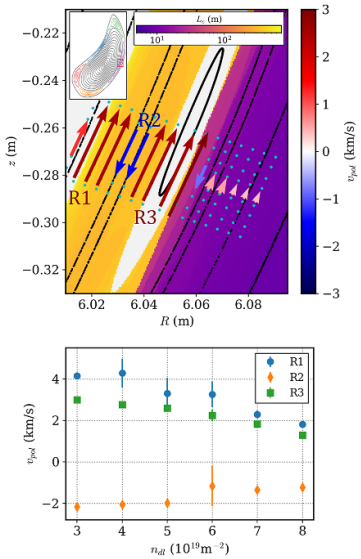

Figure 14. The top shows the multiple flow bundles measured by GPI along with the island geometry and the connection length. The flow velocity represented by the arrows is color-coded. The bottom shows the variation of the velocities in regions R1-R3 versus the line-integrated density.

by the dashed line. The measurements suggest that the plasma density is the governing quantity controlling the heat fluxes into the TSR. An increase of the radiation fraction via impurity seeding lowers the target heat fluxes considerably.

The positioning of the strike lines on the divertor targets is governed primarily by the edge rotational transform of selected magnetic configuration, see e.g. [33, 34]. In addition, HINT calculation [35] predicted the formation of a secondary strikeline at high plasma-β. This secondary strike line was experimentally observed with significant heat flux values of $Q_{tar} \approx 3-4\,\mathrm{MW\,m^{-2}}$ for $\beta_{peak} \approx 5\%$. The heat flux predictions from modeling tools, such as EMC3-Eirene and EMC3-Lite, are challenging since they depend on the *a priori* choice of the diffusivity, which can be tailored to match the observations at the target [34, 36]. However, it is generally not possible to describe up- and downstream profiles consistently [37] even with non-isotropic transport models [38].

One major effect not captured by the modeling are drifts within the edge magnetic islands [39]. Observations in W7-X show that drifts create asymmetries between the top and bottom divertor [40, 41], which varies with plasma density. Figure 13 shows the target density ratio measured by a Langmuir probe close to the strike line (figure 13(*a*)) and in the TSR (figure 13(*b*)) as a function of the line integrated density for forward and reversed magnetic field cases. Near the strike line, higher power and lower density show stronger asymmetries. The asymmetries reverse with the field reversal and are consistent with the expected $E \times B$ flow directions. Gas puff imaging (GPI) measured localized H-alpha emission on the outboard side SOL with fast cameras [42]. Stationary bi-normal flows with velocities on the order of km s^{-1} are ubiquitously found across the W7-X magnetic configuration space. In qualitative agreement with sheared $E \times B$ flows, derived from potential measurements via Langmuir probes in the island [43], GPI observed counter-streaming bi-normal flow bundles as seen in figure 14. Consistent with the density dependence of the up-down asymmetries, the flow velocity magnitudes decrease for higher plasma densities

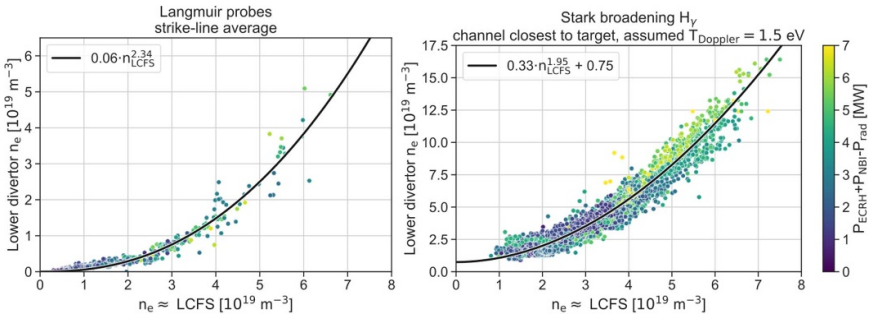

Figure 15. Shown are measurements of the divertor densities by Langmuir probes (left) and divertor spectroscopy via Stark broadening (right) against the last closed flux surface density from Thomson scattering. The power entering the scrape-off layer is color-coded. Data is averaged for 40 ms and 200 ms for the Langmuir probe and divertor spectroscopy, respectively. The database is restricted to experiments with radiated power fraction $f_{\mathrm{rad}} < 0.4$, without impurity seeding and no island chain modifications. In both plots, the black curve shows the power law fit to the respective data.

as shown in figure 14(*b*). Experiments with reversed magnetic field direction result in a reversal of the bi-normal flow directions, again indicating their drift-driven flow character. Operation at reduced magnetic fields in this last experimental campaign provided the possibility to quantitatively assess the scaling of drift effects with field strength. In the standard magnetic configuration the poloidal drift velocities were measured in the power carrying layer just outside the last closed flux surface ($r - r_{\mathrm{LCFS}} < 1$ cm) for two different field strengths. The observed flow ratio $v_{\mathrm{pol,1.8T}}/v_{\mathrm{pol,2.5T}} = 1.7$ was approx. 20% larger than the expected scaling with magnetic field ratio $2.5\,\mathrm{T}/1.8\,\mathrm{T} = 1.4$. These flows slightly shift the strike line position on the divertor target and the observed shifts are qualitatively consistent with the B-scaling of the flow velocity.

In addition, to drift-driven target asymmetries newly installed, toroidally distributed bolometer systems measured significant asymmetries in the toroidal direction. Data showed toroidal gradient length scale as low as ten or a few tens of cm in attached conditions, while typical gradient length reaching a few meters or more [44] in detached condition. The radiation asymmetry decreases with increasing density and radiated power fraction. Bolometer, Langmuir probe and spectroscopy measurements also allow to assess the radiation and divertor density scaling, which are relevant for both the power and particle exhaust capabilities. It was found that radiation shows only a weak, almost linear, scaling with upstream density (n_{LCFS}). The observed scaling extrapolates to a radiation limit of about 10 MW in unseeded, X2-heated plasmas, which are limited to line-averaged plasma densities of $n \leqslant 9 \times 10^{19}\mathrm{m}^{-2}$[45]. The other key quantity that determines the efficiency of a particular divertor configuration is the electron density $n_{(\mathrm{e,d})}$ at the target and its scaling with the upstream density. The divertor density affects the ability of exhausting both particles (through its connection to the neutral density $n_0 \propto n_{(\mathrm{e,d})}$) and power (through its connection to the radiated power $\epsilon_{\mathrm{rad}} \propto n^2_{(\mathrm{e,d})}$). Numerical predictions show that for W7-X high-recycling is suppressed [46, 47]. The experimental scaling in the standard magnetic configuration is shown in figure 15 as was measured with Langmuir probes [48] and spectroscopic assessment of Stark broadening [49]. Despite the discrepancy of the absolute magnitude of $n_{(\mathrm{e,d})}$, both diagnostics show an approximately quadratic scaling with n_{LCFS}. Similar to modeling this is significantly slower than for the high recycling scaling in tokamaks ($n_{(\mathrm{e,d})} \propto n^3_{\mathrm{LCFS}}$). However, it must be noted that more detailed investigations are required to elucidate a possible impact of diagnostic effects and a regime change in the divertor density scaling, i.e. multiple disparate scaling regimes across the accessible separatrix density range. Last, but not least, we tested reactor-relevant materials for the PFCs in W7-X by equipping selected areas of the inner heat shield and the baffle with tungsten-coated graphite tiles and with pure metal tiles [50]. First spectroscopic evidence of *WI* and *WII* line emission in the divertor plasma were measured. Significant impact of tungsten in the core was only observed during impurity accumulation in high performance experiment with peaked density profiles.

7. Summary

The W7-X stellarator has recently completed two major experimental campaigns, OP 2.2 and OP 2.3, marking an important step toward demonstrating the viability of long-pulse, steady-state fusion operation. Instead of full recommissioning before each campaign, a new operational strategy was adopted that minimized downtime and allowed two extended phases of plasma research with only short maintenance in between. This required high reliability from all technical subsystems, which was successfully achieved with failure rates below 1%. Several key upgrades supported this progress, including the operation of a prototype high-power gyrotron delivering 1.3 MW of steady-state heating, a newly developed screw-type pellet injector for long-duration fueling, and advanced feedback control systems for radiation, power stabilization, and density regulation. Together, these enhancements enabled a record discharge of 363 s with 1.8 GJ of injected heating energy, while maintaining safe divertor heat loads. In addition, innovative heating schemes allowed W7-X to explore high plasma-beta regimes, reaching unprecedented values of volume-averaged

beta and demonstrating the impact of modified equilibria. Improved confinement scenarios were also realized through central density peaking, achieved either by NBI or pellet fueling, leading to record stellarator fusion triple products comparable to tokamaks, though at smaller scale. Long-pulse pellet fueling in particular opened the path to sustaining improved confinement over much longer durations. Finally, detailed studies of the divertor and SOL highlighted the influence of drifts and plasma currents on strike-line patterns and exhaust handling, showing both agreement and limitations in present modeling approaches. Collectively, these results confirm W7-X as the leading facility for steady-state stellarator research, advancing both the scientific understanding and the technical foundation needed for future fusion reactors.

Acknowledgment

This work has been carried out within the framework of the EUROfusion Consortium, funded by the European Union via the Euratom Research and Training Programme (Grant Agreement No. 101052200–EUROfusion). Views and opinions expressed are however those of the author(s) only and do not necessarily reflect those of the European Union or the European Commission. Neither the European Union nor the European Commission can be held responsible for them.

ORCID iDs

O. Grulke 0000-0001-7879-8671
S. Bannmann 0000-0003-0772-9278
S. Bozhenkov 0000-0003-4289-3532
C. Büschel 0009-0002-3864-8008
O.P. Ford 0000-0002-5646-4758
D. Hartmann 0000-0002-3511-6500
C. Killer 0000-0001-7747-3066
A. Langenberg 0000-0002-2107-5488
V. Perseo 0000-0001-8473-9002
T. Romba 0000-0002-2727-9385
F. Scharmer 0009-0005-2310-5731
T. Stange 0000-0003-4154-1455
A. von Stechow 0000-0003-0277-4600
A. Tsikouras 0009-0008-9677-3302

References

[1] Ponomarenko S. *et al* 2024 Experimental results of the novel 1.5-mw-class 140-ghz continuous-wave gyrotron for the Wendelstein 7-X stellarator *IEEE Electron Device Lett.* **45** 2550–3
[2] Meitner S.J., Baylor L.R., Gebhart T.E., Harris J.H., McGinnis W.D., Bjorholm T.P. and Logan K.G. 2020 Design of a continuous pellet fueling system for Wendelstein 7-X *IEEE Trans. Plasma. Sci.* **48** 1585–90
[3] Grulke O. *et al* 2024 Overview of the first Wendelstein 7-X long pulse campaign with fully water-cooled plasma facing components *Nucl. Fusion* **64** 1
[4] Zanini M. *et al* 2019 Eccd operations in the second experimental campaign at W7-X *EPJ Web Conf.* **203** 02013
[5] Beidler C. *et al* 2001 The helias reactor HSR4/18 *Nucl. Fusion* **41** 1759–66
[6] Wolf R.C., Beidler C.D., Dinklage A., Helander P., Laqua H.P., Schauer F., Pedersen T.S. and Warmer F., (Wendelstein 7-X Team) 2016 Wendelstein 7-X program-demonstration of a stellarator option for fusion energy *IEEE Trans. Plasma. Sci.* **44** 1466–71
[7] Drevlak M., Geiger J., Helander P. and Turkin Y. 2014 Fast particle confinement with optimized coil currents in the W7-X stellarator *Nucl. Fusion* **54** 073002
[8] Marushchenko N.B., Aleynikov P., Beidler C.D., Dinklage A., Geiger J., Helander P., Laqua H.P., Maassberg H. and Turkin Y. (Wendelstein 7-X Team) 2019 Reduced field scenario with X3 heating in W7-X *EPJ Web Conf.* **203** 01006
[9] Beurskens M.N.A. *et al* 2021 Ion temperature clamping in Wendelstein 7-X electron cyclotron heated plasmas *Nucl. Fusion* **61** 116072
[10] Bozhenkov S.A. *et al* 2020 High-performance plasmas after pellet injections in Wendelstein 7-X *Nucl. Fusion* **60** 066011
[11] Langenberg A. *et al* 2024 Achieving stationary high performance plasmas at Wendelstein 7-X *Phys. Plasmas* **31** 0199958
[12] Ford O.P. *et al* 2024 Turbulence-reduced high-performance scenarios in Wendelstein 7-X *Nucl. Fusion* **64** 086067
[13] Bannmann S. *et al* 2024 Particle transport in reduced turbulence neutral beam heated discharges at Wendelstein 7-X *Nucl. Fusion* **64** 106015
[14] Wappl M., Bozhenkov S.A., Andreeva T., Bannmann S., Smith H.M. and Wolf R.C. (the W7-X Team) 2025 Experimental power balance study on turbulent heat transport at Wendelstein 7-X *Plasma Phys. Control Fusion* **67** 075025
[15] Thienpondt H., García-Regaña J.M., Calvo I., Acton G. and Barnes M. 2024 Influence of the density gradient on turbulent heat transport at ion-scales: an inter-machine study with the gyrokinetic code stella *Nucl. Fusion* **65** 016062
[16] Bannmann S. *et al* 2026 Tokamak level performance in the optimized stellarator Wendelstein 7-X with stable peaked density profiles *Phys. Rev. E* accepted (https://doi.org/10.1103/q59k-8m26)
[17] Baldzuhn J. *et al* 2019 Pellet fueling experiments in Wendelstein 7-X *Plasma Phys. Control. Fusion* **61** 095012
[18] Baldzuhn J. *et al* 2020 Enhanced energy confinement after series of pellets in Wendelstein 7-X *Plasma Phys. Control. Fusion* **62** 055012
[19] Beurskens M.N.A. *et al* 2022 Confinement in electron heated plasmas in Wendelstein 7-X and ASDEX Upgrade; the necessity to control turbulent transport *Nucl. Fusion* **62** 016015
[20] Litaudon X. *et al* 2024 Long plasma duration operation analyses with an international multi-machine (tokamaks and stellarators) database *Nucl. Fusion* **64** 015001
[21] Xanthopoulos P., Merz F., Görler T. and Jenko F. 2007 Nonlinear gyrokinetic simulations of ion-temperature-gradient turbulence for the optimized Wendelstein 7-X stellarator *Phys. Rev. Lett.* **99** 035002
[22] Alcusón J.A., Xanthopoulos P., Plunk G.G., Helander P., Wilms F., Turkin Y., von Stechow A. and Grulke O. 2020 Suppression of electrostatic micro-instabilities in maximum-j stellarators *Plasma Phys. Control Fusion* **62** 035005
[23] Baehner J.-P. *et al* 2021 Phase contrast imaging measurements and numerical simulations of turbulent density fluctuations in gas-fuelled ecrh discharges in Wendelstein 7-X *J. Plasma Phys.* **87** 905870314
[24] Wegner T. *et al* 2020 Impact of the temperature ratio on turbulent impurity transport in Wendelstein 7-X *Nucl. Fusion* **60** 124004

[25] Proll J.H.E., Helander P., Connor J.W. and Plunk G.G. 2012 Resilience of quasi-isodynamic stellarators against trapped-particle instabilities *Phys. Rev. Lett.* **108** 245002
[26] Helander P., Newton S.L., Mollén A. and Smith H.M. 2017 Impurity transport in a mixed-collisionality stellarator plasma *Phys. Rev. Lett.* **118** 155002
[27] Huang Z. *et al* 2021 The Wendelstein 7-X phase contrast imaging diagnostic *J. Instrum.* **16** 01014
[28] Litaudon X. *et al* (The IEA Coordination on International Challenges on Long duration Operation (CICLOP) group) 2025 Investigating long-duration plasma operation with the international multi-machine database *30th IAEA Fusion Energy Conference (FEC2025)* (*Chengdu, People's Republic of China*, *13–18 October 2025*)
[29] Cu-Castillo H. *et al* 2026 Significance of microtearing turbulence in turbulence-reduced high-density-gradient plasmas in Wendelstein 7-X *Phys. Rev. Lett.* (https://doi.org/10.1103/nd3p-yb9t)
[30] Jenko F., Dorland W., Kotschenreuther M. and Rogers B.N. 2000 Electron temperature gradient driven turbulence *Phys. Plasmas* **7** 1904–10
[31] Perseo V. *et al* 2025 Increased power operation with water-cooled divertors at Wendelstein 7-X *5th IAEA Technical Meeting on Divertor Concepts, 2025* (*Vienna, Austria*, *28–31 October 2025*)
[32] Naujoks D. *et al* 2026 Heat load mitigation studies in the W7-X stellarator experiment *Nucl. Fusion* **64** 112002
[33] Gao Y. *et al* 2019 Effects of toroidal plasma current on divertor power depositions on Wendelstein 7-X *Nucl. Fusion* **59** 106015
[34] Kharwandikar A. 2025 Power exhaust investigations in the W7-X island divertor *PhD Thesis* University Greifswald
[35] Knieps A. *et al* 2022 Plasma beta effects on the edge magnetic field structure and divertor heat loads in Wendelstein 7-X high-performance scenarios *Nucl. Fusion* **62** 026011
[36] Feng Y. *et al* 2021 First attempt to quantify W7-X island divertor plasma by local experiment-model comparison *Nucl. Fusion* **61** 106018
[37] Bold D., Reimold F., Niemann H., Gao Y., Jakubowski M., Killer C. and Winters V.R. (the W7-X Team) 2022 Parametrisation of target heat flux distribution and study of transport parameters for boundary modelling in W7-X *Nucl. Fusion* **62** 106011
[38] Bold D., Reimold F., Niemann H., Gao Y., Jakubowski M., Killer C., Winters V.R. and Maaziz N. (the W7-X Team) 2024 Impact of spatially varying transport coefficients in emc3-eirene simulations of W7-X and assessment of drifts *Nucl. Fusion* **64** 126055
[39] Feng Y., Sardei F., Grigull P. and Herre G. 1999 Drift effects in W7-AS limiter and island divertor configurations *J. Nucl. Mater.* **266-269** 928–33
[40] Hammond K.C. 2019 Drift effects on W7-X divertor heat and particle fluxes *Plasma Phys. Control. Fusion* **61** 125001
[41] Kriete D.M. and Fusion N. 2023 Effects of drifts on scrape-off layer transport in W7-X *Nucl. Fusion* **63** 026022
[42] Terry J.L. 2024 Realization of a gas puff imaging system on the Wendelstein 7-X stellarator *Rev. Sci. Instrum.* **95** 093517
[43] Killer C., Cipciar D., Baek S.G., Ballinger S.B., von Stechow A., Terry J.L. and Grulke O. (the W7-X Team) 2025 Electric fields and stationary drift flows in the island divertor SOL of Wendelstein 7-X *Nucl. Fusion* **65** 056026
[44] Partesotti G. 2024 Assessing the toroidal radiation distribution at Wendelstein 7-X by combining Gaussian Process Tomography and field line mapping *Nucl. Mater. Energy* **41** 101823
[45] Reimold F. 2024 Power & particle exhaust limitations in W7-X and its relation to density build-up in the divertor *Conf. on Plasma Surface Interaction (PSI), 2024* (*Marseille, France*, *12–17 May 2024*)
[46] Feng Y., Kobayashi M., Lunt T. and Reiter D. 2011 Comparison between stellarator and tokamak divertor transport *Plasma Phys. Control. Fusion* **53** 024009
[47] Maaziz N., Reimold F., Winters V.R., Bold D., Feng Y. and Perseo V. 2025 Investigating the role of divertor geometry on density build-up in the island divertor *Nucl. Mater. Energy* **42** 101886
[48] Pandey A. and Fusion N. 2024 Pop-up Langmuir probe diagnostic in the water cooled divertor of Wendelstein 7-X *Rev. Sci. Instrum.* **95** 043503
[49] Henke F. 2025 Development and experimental validation of impurity line ratio spectroscopy for divertor plasmas at W7-X *PhD Thesis* University Greifswald
[50] Naujoks D. 2023 Performance of tungsten plasma facing components in the stellarator experiment W7-X: recent results from the first OP2 campaign *Nucl. Mater. Energy* **37** 101514